Materials Research. 2017; 20(5): 1309-1316
DOI: http://dx.doi.org/10.1590/1980-5373-MR-2017-0290

Structure and Physical Properties of the $LaBiFe_2O_6$ Perovskite Produced by the Modified Pechini Method

Johny Andrés Jaramillo Palacio[a], Elixir William Barrera Bello[a,b], Julián Andrés Munévar Cagigas[c], Oscar Arnache[d], David A. Landínez-Téllez[a], Jairo Roa-Rojas[a]*

[a]Grupo de Física de Nuevos Materiales, Departamento de Física, Universidad Nacional de Colombia, AA 5997, Bogotá DC, Colombia
[b]Departamento de Ciencias Básicas, Universidad Católica de Colombia, Bogotá DC, Colombia
[c]Laboratory for Muon Spin Spectroscopy, Paul Scherrer Institut, CH-5232, Villigen PSI, Switzerland
[d]Grupo de Estado Sólido, Instituto de Física, Universidad de Antioquia, AA 1226, Medellín, Colombia

Received: March 16, 2017; Revised: March 22, 2017; Accepted: July 03, 2017

In this paper the synthesis of the $LaBiFe_2O_6$ material by the modified Pechini method is reported. Structural, morphologic, magnetic and optic experimental studies were performed. Rietveld refinement of x-ray diffraction patterns revealed that $LaBiFe_2O_6$ crystallizes in an orthorhombic perovskite structure (space group *Pnma, # 62*). Scanning electron microscopy images showed the nanometric feature of grains. X-ray dispersive spectroscopy permitted to infer the obtaining of the $LaBiFe_2O_6$ expected stoichiometry. Results of magnetic susceptibility as a function of temperature and field magnetization evidenced mixed ferromagnetism and superparamagnetism behavior at $T=300$ *K*. Mössbauer spectroscopy supported the superparamagnetic and ferromagnetic responses as a result of the nanogranular morphology and anisotropy effects. Spectrum of diffuse reflectance suggest that this material behaves as a semiconductor with energy gap $E_g=2.13$ *eV*.

Keywords: *Modified Pechini method, double perovskite, ferromagnetic, semiconductor*

1. Introduction

The Pechini method for the synthesis of materials is a relatively new technique that, at first, was implemented for deposition of films base on lead and alkaline earth titanates and niobates applied to the technology of dielectrics and capacitors[1]. In the last years this method has enabled synthesis $BaTiO_3$ nanopowders[2] and other perovskite-like materials[3]. The biggest advantage of this method lies in its simplicity and in the almost completely independence of the process conditions of the chemistry of positive ions contained in the final material and a low sintering temperature, resulting in obtaining powders oxides formed by nanometer sized crystals. On the other hand, this method includes some disadvantages such as the use of glycol toxic ethylene and significant volumes of organic reagents of the product, lack of complexes stable citrus elements such as bismuth, as well as partial or complete regeneration of certain components during pyrolysis of polymer gel, such as copper and ruthenium, among others. In order to solve some of the disadvantages of this method in the synthesis of lanthanide oxides, recently it has been applied the so-called *modified Pechini method*, by which it has achieved a further reduction in the size of the obtained crystals[4]. This method can be applied in the processes of synthesis of simple perovskites based on lanthanum, with crystallographic single phase, in nanometric size grains strongly coupled to form lamellar structures ranging from sizes with tens of nanometers up to several micrometers[5]. So far, there are very few reports of double perovskites produced through this technique[6-7]. Double perovskites are materials extensively studied due to the potential that their generic formula $AA'MM'O_6$, where A- and A'-cation, and M- and M'-cations can be the same or different type, provides to modify the structure and, consequently, the physical properties of this family of compounds, by introducing various elements in sites A and M of that formula[8-9]. The novel double perovskite material $LaBiFe_2O_6$ has recently been reported as a possible biferroic with ferromagnetic and ferroelectric response at room temperature[10]. The aim of this work is to study the crystal structure, morphology, composition, and magnetic and optic characterizations of $LaBiFe_2O_6$ perovskite samples produced by applying the modified Pechini method, and to analyze the effect of the nanometric size grain on the magnetic and electric properties compare with that published for this materials synthesized by the solid state reaction technique.

2. Experimental

$LaBiFe_2O_6$ nanopowder samples were produced by the modified Pechini method[4]. Aldrich La_2O_3 (99.99%),

* e-mail: jroar@unal.edu.com

$Bi(NO_2)_2.5H_2O$ (Aldrich 99.9%) and $Fe(NO_2)_2.9H_2O$ (Aldrich 99.99%) were added separately in hot nitric acid solutions, which was selected as chelating agent (CA). First, the lanthanum oxide was separately mixed with nitric acid and heated up to obtain a clear aqueous solution. This solution was mixed with the Fe and Bi based precursor previously dissolved in water. Then, the nitric acid is added in a *1:1* CA-to-metal molar ratio, and submitted to a strong magnetic stirring for *3 hours*. For the polyesterification process, ethylene glycol was used as esterification agent (EA). Ethylene-glycol was added in a *1:2* CA-EA ratio followed by slow evaporation of water at *373 K* for *15 hours* in constant magnetic stirring. The organic precursor was annealed in two steps, first at *573 K* for *3 h* and second at *1023 K* for *1 h* to obtain nanopowder with perovskite structure. The determination of the crystal structure of the $LaBiFe_2O_6$ samples were carried out by means X-ray diffraction experiments through a PANalytical X'pert PRO diffractometer ($\lambda_{CuK\alpha}$*=1.54064 Å*). The analysis of the experimental data was performed from Rietveld refinement by using the GSAS+EXPGUI code[11], through which it is possible to obtain directly the most relevant structural parameters and the corresponding space group. In order to examine the surface morphology of the samples, Scanning Electron Microscopy (SEM) images were taken by using VEGA 3 TESCAN equipment. A semi-quantitative comparison of the nominal stoichiometry of the samples was established through application of the Energy Dispersive X-ray Spectroscopy (EDS) microprobe coupled to the electron microscope. With the purpose of analyzing the magnetic response of the material, measurements of susceptibility as a function of temperature and magnetization hysteresis curves were performed on Quantum Design MPMS magnetometer. Zero Field Cooling (ZFC) and Field Cooled (FC) procedures were carried out to determine the temperature dependence of the susceptibility on the application magnetic fields *H= 500, 2000* and *10000 Oe*. Hysteresis loops of magnetization as a function of applied fields were recorded at *T=50, 200* and *300 K*. This solid-reacted material was previously reported as semiconductor[10], then diffuse reflectance measurements were examined by means a VARIAN Cary 5000 UV-Vis-NIR spectrophotometer. Finally, Mössbauer measurements were performed by means a *100mCi 57Co* source in an Rh matrix, which was driven at a constant acceleration in a triangular mode at room temperature. The spectra were recorded in 512 channels and the Lorentzian lines of the folded data were fitted using Recoil software[12]. The spectrometer was calibrated with the room temperature spectrum of α-Fe foil. All isomer shift values were expressed with respect to the centroid of this spectrum.

3. Results and Discussion

The structural analysis of the material is made from the predictions of the Structure Prediction Diagnostic Software (SPuDS)[13], which gives the most probable spatial groups and the respective Wyckoff positions of all the ions for a new material. These predictions are used as input data for the simulation of diffraction patterns in the Powdercell (PCW)[14], in which it is possible to establish all the diffractive planes, with their respective Miller indices and 2θ positions, for each spatial group predicted by the SPuDS. Finally, through the application of the GSAS code and its respective graphic interface EXPGUI[11], the simulated patterns are compared with the experimental diffractogram in a refinement process that allows determining to which of the probable spatial groups corresponds the experimental XRD pattern. Likewise, through refinement, all the structural parameters are obtained and all the diffractive planes are indexed, since the code allows the analysis of the shape and structure factors during the refinement process.

The XRD pattern for the $LaBiFe_2O_6$ samples produced by the modified Pechini method is exemplified in Figure 1, where symbols represents the experimental data, the red line is associated to the simulated diffractogram, the blue line indicates the experimental background and the green line is the difference between the theoretical and experimental patterns. The reliability parameters associated to the refinement quality where χ^2*=2.81*; *R(F²)=0.0323;* R_p*=0.0306* and R_{wp}*=0.0401*. This can be said from the analysis that the $LaBiFe_2O_6$ material crystallizes in an orthorhombic perovskite, *Pnma (#62)* space group, with lattice parameters *a=5.5786(3) Å*, *b=7.8649(8) Å* and *c=5.5583(7) Å*, and respective angles α=β=γ*=90.0°*. The appearance of the diffraction peaks (111) and (311) constitutes a strong indication that the La^{3+} and Bi^{3+} cations are placed in an orderly manner into the structure along the crystallographic directions.

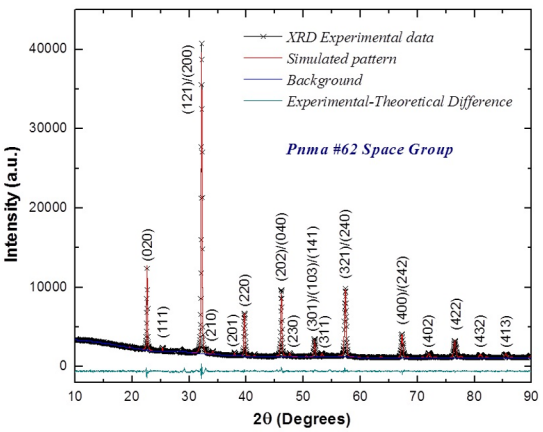

Figure 1. Comparison between the refined XRD data and the simulated pattern for the $LaBiFe_2O_6$ material.

It is expected that the *Pnma* space group corresponds to simple perovskites as $CaTiO_3$[15]. This orthorhombic structure is characterized by the Glazer notation $a^-b^+a^-$, which is characterized by two angles of rotation with quite similar

magnitude and opposite directions and corresponds to an increase of $\sqrt{2}$ in the *a=b* cell parameter and doubling the value of the *c* parameter when compared with the cubic $Pm\bar{3}m$ perovskite. The crystallization of double perovskite materials in this structure probably occurs when the ionic radii $r_A \approx r_{A'}$. In our $LaBiFe_2O_6$ material there is a great similarity between the ionic radii $r_{La^{3+}}=1.22$ Å and $r_{Bi^{3+}}=1.24$ Å.

In order to properly describe the crystallographic structure the concept of Wyckoff positions is used[16], as presented in Table 1.

Table 1. Relevant lattice parameters for the $LaBiFe_2O_6$ complex perovskite in the *Pnma* space group.

		Atomic coordinates		
Atom	*Wyckoff positions*	*x*	*y*	*z*
La, Bi	4c	0.52003	0.25000	0.50333
Fe	4a	0.50000	0.00000	0.00000
O(1)	4c	-0.00344	0.25000	0.44753
O(2)	8d	0.26671	0.04962	0.72421

Eight oxygen atoms are sited in the *ac*-plane, corresponding to the *8d* Wyckoff positions, and four oxygen atoms are along the *b*-axis, in the *4c* Wyckoff positions. This splitting of the oxygen in two different Wyckoff orbits constituted an evidence of the occurrence of a structural transition from a cubic phase $Pm\bar{3}m$ to the orthorhombic *Pnma*, since in a cubic one Wyckoff position for the oxygen atoms is sufficient to describe the structure.

It is clear from the Glazer notation $a^-b^+a^-$ that octahedral distortions are expected with tilting in antiphase along the *a*-axis and tilting in-phase along the *b*-axis, where *a* and *b* represents the pseudocubic sub-cell lengths[17]. These octahedral distortions are easily observable in Figure 2. Figure 2a shows the FeO_6 octahedra in the *b-c* crystallographic plane of the structure, which it should not be confused with any plane formed by the pseudocubic axes. Furthermore, Figure 2b shows the cell seen from the *a-c* crystallographic plane. In Figures 2a and 2b the octahedra tilting can be clearly observed.

The irregular shape of the octahedra can be analyzed from Figures 2c and 2d, where it can be determined that the distances between $\boldsymbol{Fe^{3+}}$ **cations and** $\boldsymbol{O^{2-}}$ anions adopt different values along the octahedral axes, as follows: *1.987 Å* between *Fe-O(1)*, and *1.985 Å* and *2.044 Å* between *Fe-O(2)*. This octahedral symmetry justifies the difference between the Wyckoff positions of the *O(1)* and *O(2)* anions represented in Table 1.

The mean size of the crystalline domains was analyzed by the application of the Scherrer formula, which is given by

$$\tau_{hkl} = \frac{\kappa\lambda}{\beta\cos\theta}, \qquad (1)$$

where, τ_{hkl} is the mean size of the ordered crystalline domains (crystallite), which depends of the *hkl* direction; κ represents a dimensionless has a typical value close to *0.9*, but depends of the crystallite shape; $\lambda=1.54056$ Å is the X-ray wavelength, β is the line broadening at half the maximum intensity and θ corresponds to the Bragg angle. The mean size of the crystallite obtained by the Scherrer equation was $\tau_{hkl}=44.2 \pm 4.1$ *nm*. The crystallite size is calculated by the equation 1 as showed in Figure 3.

Another way to calculate the average crystallite size is through the equation applied by the GSAS code during the process of Rietveld refinement of XRD experimental data. This method is carried out by considering the Debye-Scherrer cone in the scattering angle *2θ*. The applied expression is

$$\tau = \frac{18000\kappa\lambda}{\pi X'}, \qquad (2)$$

where, $\kappa \approx 0.9$ is the Scherrer constant, $\lambda=1.54056$ Å is the X-ray wavelength and $X' = X + P_{tec}$ is the Lorentzian coefficient of particle size and anisotropy factor for the parallel crystallite size and *X* for the perpendicular crystallite size. The average crystallite size given by the GSAS refinement was $\tau=52.2\pm4.2$ *nm*, which is close to that obtained through the direct application of the Scherrer formula.

The granular surface topology of the samples is exemplified in the micrographs of Figure 4. Perfectly defined polyhedral grains of nanometric dimensions are observed in Figure 4. It is not clear necking between the grains as a result of a possible diffusion, which is explained by the high sintering temperature (*1023 K*) of the material after the synthesis process by the modified Pechini method.

The mean grain size was determined by the Average Grain Intercept (AGI) method, by drawing a set of randomly Positioned line segments on the SEM image, counting the number of times each line segment intersects a grain boundary, and finding the Intercepts ratio of length to line. Thus, the average grain size was estimated at *373 ± 42 nm* (Figure 5), which is a much smaller size than the reported value for samples produced by solid state reaction[10].

The semiquantitave stoichiometry of samples was analyzed the EDS microprobe coupled to SEM equipment. Figure 6 exemplifies the EDS spectra from electron beams incident on the different surface grains of the samples. From the results it was established that the samples contain the stoichiometry expected from the nominal formula up in 98 %.

The magnetic susceptibility response as a function of temperature on the application of intensity fields *H=500 Oe, 2000 Oe* and *10000 Oe* is presented in Figure 7. For each value of intensity of applied magnetic field *H*, the sample was first cooled in absence of field. Then *H* was applied and susceptibility was measured while the temperature was increased in the procedure known as ZFC recipe. In the FC prescription, the sample was cooled and measured under application of *H*. A strong irreversibility was observed for all values of applied field, which is an indicative of the occurrence

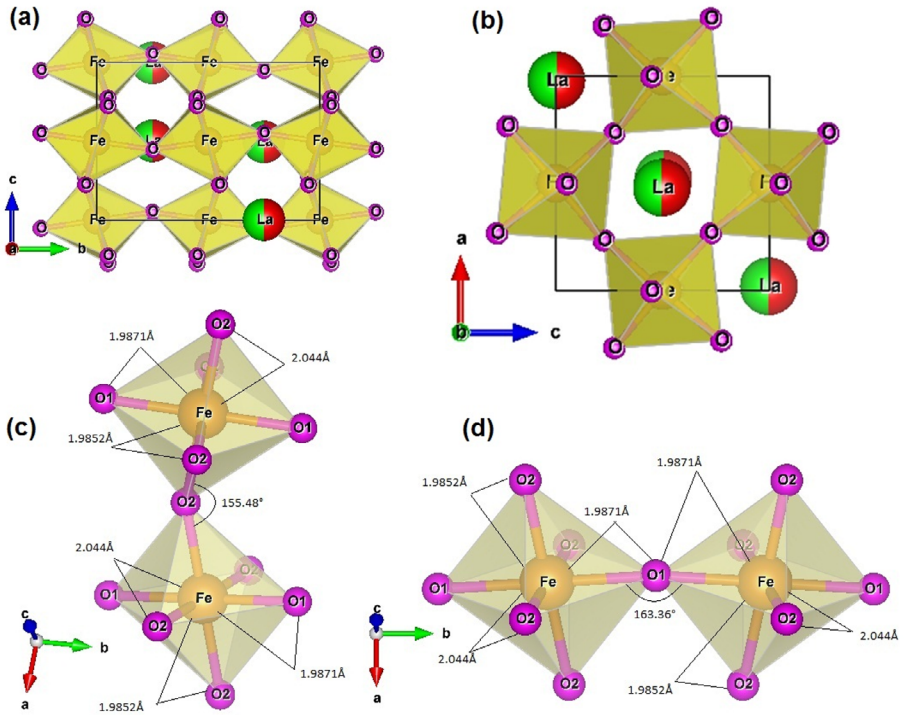

Figure 2. Structure and octahedral distortions of the $LaBiFe_2O_6$ material in the *Pnma* space group.

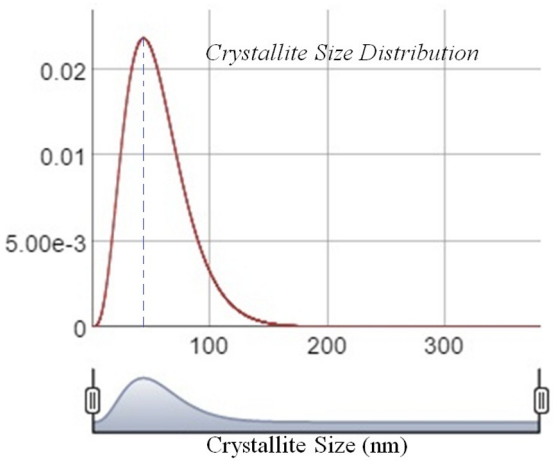

Figure 3. Mean crystallite size calculated by the Scherrer equation.

of some kind of disorder that facilitates the freezing of the domains of magnetic spins in the ZFC procedure.

One possible cause of this behavior of magnetically frustrated system is the cationic disorder of La^{3+} and Bi^{3+} atoms at the A and A' sites of the double perovskite. Meanwhile, this possibility is ruled out because the Rietveld refinement permitted to identify the reflection peaks (111) and (311), which constitute an evidence of formation of a FCC type structure that can only take place when the $\boldsymbol{La^{3+}}$ **and** $\boldsymbol{Bi^{3+}}$ cations are alternately arranged along the A and A' sites of the structure.

The presence of sub-micrometric grain-size can introduce border and surface effects, as well as the possibility of formation of independent magnetic domains which can to give rise relevant contribution to the frustrated nature of the material. For all applied magnetic fields a strong ferromagnetic behavior is observed in the magnetic susceptibility in all temperature regimes studied ($50\ K<T<325\ K$), so it is expected that the Curie temperature occurs for values of temperature well above room temperature. An interesting feature involves the no occurrence of anomalies or magnetic pseudo-transitions in the susceptibility for temperature values around $T=258\ K$, as reported for solid reacted samples[10].

In the picture of Figure 8, a clear ferromagnetic behaviour of magnetization measurements as a function of applied field at $T=50\ K$, $200\ K$ and $300\ K$ is presented. It is observed that the lower remnant magnetization and coercive field occur at $T=50\ K$, at $T=200\ K$ remnant magnetization and coercive field are higher and then these values decrease considerably for $T=300\ K$, as showed in Figure 8.

In none of the magnetic hysteresis curves shown in Figure 7 the saturation magnetization (M_S) is reached, but it is possible to infer that most M_S could take place for $T=50\ K$ and lower for $T=300\ K$. At temperatures close to room temperature, the behavior of the hysteresis curve (under application of high magnetic fields) reveals a linear trend with no evidence of saturation. Due the nanogranularity of the ferromagnetic material, surface effects gain importance, so that the anisotropy and the magnetic monodomains

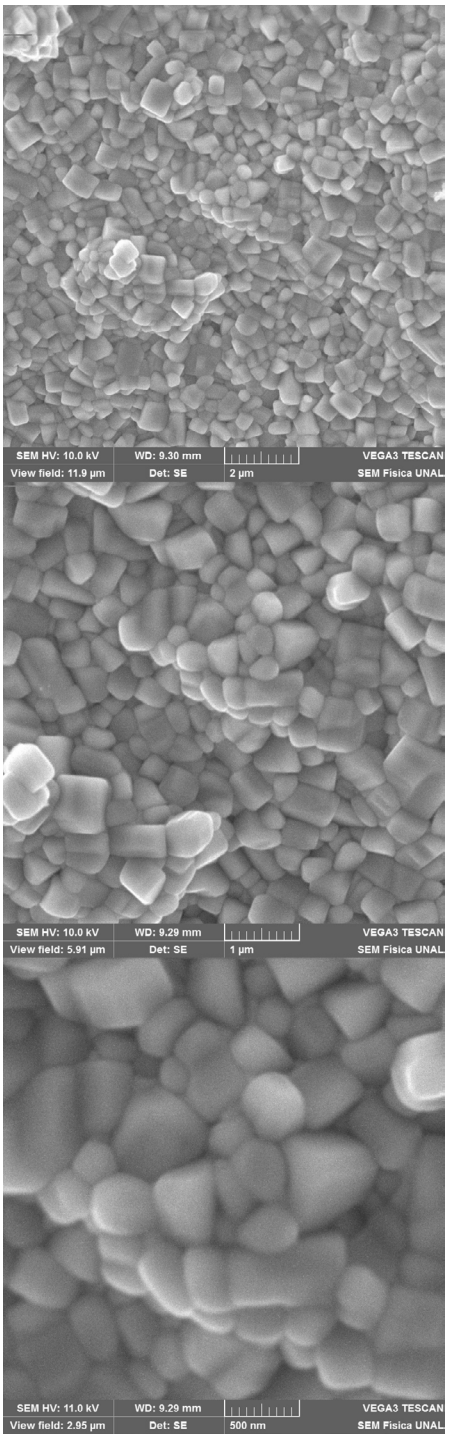

Figure 4. Granular surface structure of sample in the powder form obtained from SEM images with magnifications (a) 15000X, (b) 32500X and (c) 65000X.

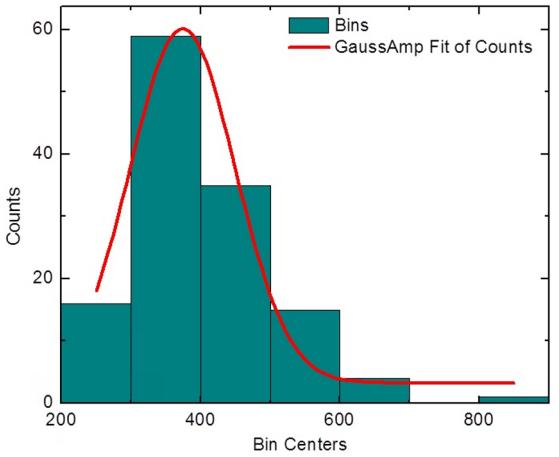

Figure 5. Determination of the mean grain size by the AGI method from the image of figure 4.

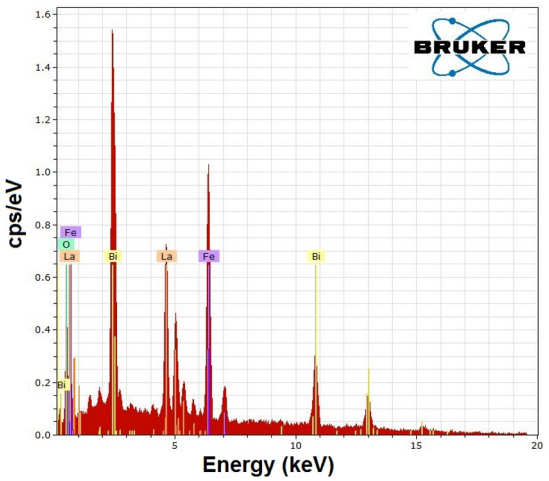

Figure 6. EDS spectrum observed for the $LaBiFe_2O_6$ double perovskite.

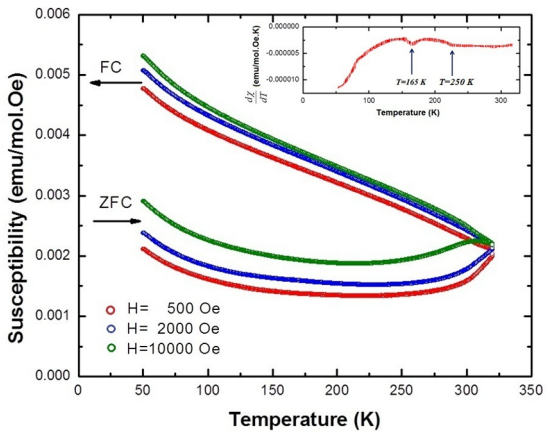

Figure 7. Magnetic susceptibility as a function of temperature for the $LaBiFe_2O_6$ material on the application of *H=500 Oe*, *2000 Oe* and *10000 Oe*. The inset shows the temperature derivative of susceptibility for *H=500 Oe*.

induced in the surface are more relevant than the exchange mechanisms, resulting in a volumetric ferromagnetic response mixed with superparamagnetic effects, which would justify the linear trend of the hysteresis curve in the regime of high magnetic field strengths for *T=300 K*. Likewise, this

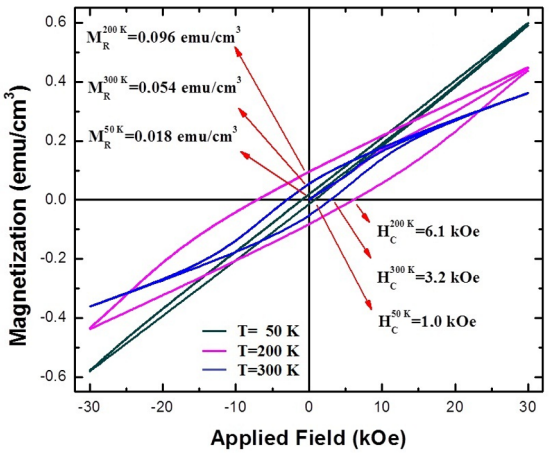

Figure 8. Magnetization as a function of applied field measured at the temperatures *T=50 K*, *200 K* and *300 K*.

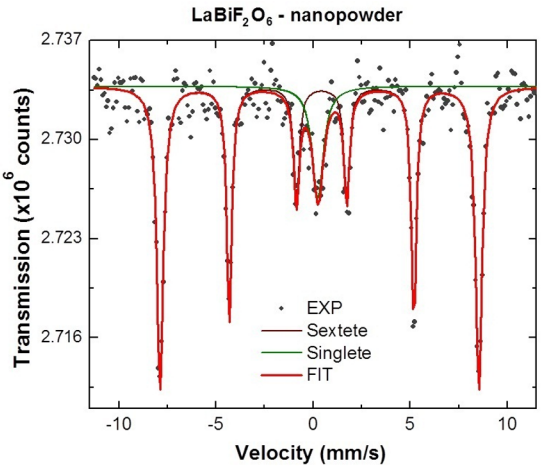

Figure 9. Mössbauer spectrum for the $LaBiFe_2O_6$ perovskite and applied fitting model.

would explain decreasing in values of coercivity field and remnant magnetization when temperature is increased from *200 K* to *300 K*.

From the curves of susceptibility as a function of temperature (Figure 7), it is expected that at lower temperatures a greater number of magnetic moments align in the direction of the applied field. In Figure 8 it can be observed that indeed the magnetization is greater at low temperatures. Furthermore, in the inset of Figure 7, the curve of temperature derivative of susceptibility shows that there is a change of concavity at *T = 165 K*. This anomaly may be related with nanoscopic mechanisms that modify the ferromagnetic domains, increasing partially the values of the magnetic parameters (coercive field and remnant magnetization). At higher temperatures, surface effects that give rise to the superparamagnetic nature inhibit the ferromagnetic order, decreasing values of the magnetic parameters.

In order to elucidate the nature of eventual local induced magnetic effects and the vibrational state of Fe^{3+} cations behavior in the structure, measurements of Mössbauer spectroscopy were carried out with the application of a Lorentzian model as showed in Figure 9. The reduced uncertainties calculated from the covariance matrix gives $\chi^2 = 0.565$.

The applied model showed the occurrence of a singlet related with a relevant fraction (*14%*) of superparamagnetic response, which is attributed to the nanometric character of grains observed in Figure 4 and analyzed in Figure 5[18]. On the other hand, a sextet was clearly identified, related to the $\boldsymbol{Fe^{3+}}$ in the octahedral coordination. The hyperfine parameters from the fits are reported in Table 2.

From Table 2, it is noted that, the high magnetic field *(~51 T)* imply that this kind of perovskite has a magnetic behavior at room temperature, which are due to the magnetic interactions of the two different types of magnetic ions: $\boldsymbol{Fe^{3+}}$ **and** $\boldsymbol{(La/Bi)^{3+}}$, and the competition between *Fe-Fe*, *(La/Bi)-Fe* and *(La/Bi)-(La/Bi)* interactions in different magnetic networks. This means that the interactions between the *Fe* cations mediated by the oxygen anions are directly affected by the bond lengths and bond angles, which in turn affect the magnitude of the hyperfine field[19]. The above results are in good agreement with those observed in the structural and magnetic analysis.

Table 2. Hyperfine parameters of $LaBiFe_2O_6$ derived from the fit of room temperature Mössbauer spectra.

δ *(mm/s)*	ε *(mm/s)*	Γ *(mm/s)*	$H_i(T)$	χ^2
		Sextet		
0.25±0.01		0.34±0.01		
		Singlet		
0.38±0.01	-0,06±0,01	0.18±0.01	50.9±0.1	0.5648

The gap energy was experimentally estimated by the Diffuse Reflectance technique. Results are shown in Figure 10. Three peaks are observed in Figure 10a for wave lengths λ_1*=332 nm,* λ_2*=604 nm* and λ_3*=799 nm*. These peaks correspond to energies E_1*=3.73 eV,* E_2*=2.05 eV* and E_3*=1.55 eV* due to electronic excitations caused by electronic transitions from the valence band to the conduction bands.

In the spectrum for the $LaBiFe_2O_6$ complex perovskite, these energies are related to the symmetry of the atomic positions in the space group *Pnma (#62)* by the transitions O_{2p}-La_{5d}, O_{2p}-Fe_{3d} and O_{2p}-Bi_{6p}[20] on the irreducible representation of vibrations given by

$$\Gamma = 5\ Raman\ Vibration\ Modes + 7B_{1u} + 9B_{2u} + 9B_{3u}, \quad (3)$$

where, the first term correspond to five vibration modes which are observable by Raman spectroscopy and the $7B_{1u}$, $9B_{2u}$ and $9B_{3u}$ modes appear as three peaks measured through UV-Vis-IR spectroscopy.

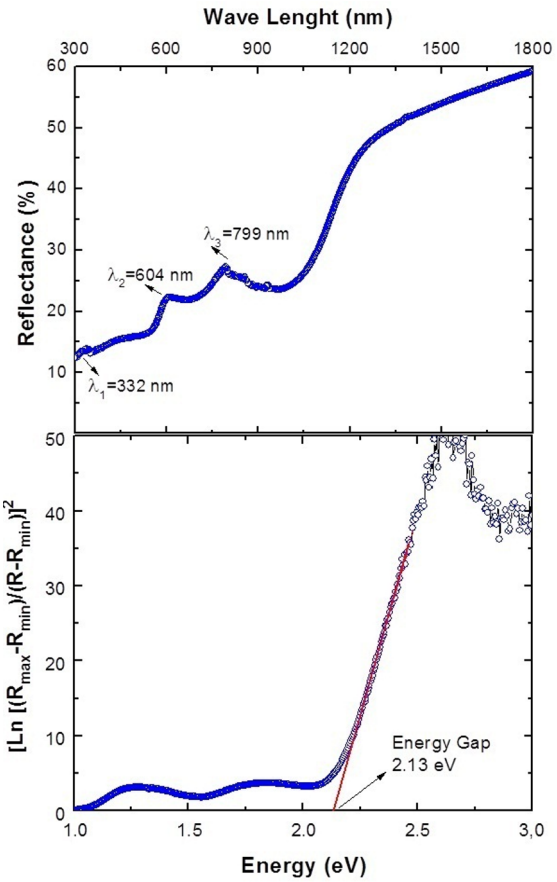

Figure 10. Diffuse reflectance measurements in the $LaBiFe_2O_6$ samples: a) % reflectance as a function of wave length and b) Kubelka-Munk analysis.

For the determination of the energy gap the method of Kubelka-Munk analysis is applied in the way as implemented by V. Kumar et al.[21].

The absorption coefficient is given by

$$\alpha_b = \frac{B(h\nu - E_g)^n}{h\nu}, \qquad (4)$$

where, $h\nu$ is the absorbed energy, B is the absorption constant, E_g represents the gap energy and $n=1/2$ or $n=2$ if there are direct or indirect semiconductor transitions, respectively. The energy gap is equivalent to the absorbed energy when $\alpha_R = \ln R$, where R is the measured reflectivity relative to the unity. By representing the $\left[\ln\frac{R_{max}-R_{min}}{R-R_{min}}\right]^2$ vs $h\nu$, it is possible to determine the gap energy as showed in Figure 10b. The results of diffuse reflectance are related to the chemical structure of the material. In the case of $\boldsymbol{Fe^{3+}}$, the valence and conduction bands present a splitting of the *3d*-Fe levels in the crystal field as a result of the octahedral coordination of the FeO_6. From the analysis of the Diffuse Reflectance spectrum, the obtained energy gap was *2.13 eV*, which corresponds to semiconductor behaviour. The difference of this value as compared with reports for $LaFeO_3$ (*2.67 eV*)[22] and $BiFeO_3$ (*2.81 eV*)[23] is partially caused by the occurrence of three different Fe_{3d}-O_{2p} bonds into the FeO_6 octahedra: *1.987 Å* for *Fe-O(1)*, and *1.985 Å* and *2.044 Å* for *Fe-O(2)*. Likewise, the interatomic distances of the *La-O* and *Bi-O* bonds are not symmetrical because of the occurrence of octahedral distortions.

4. Conclusions

The $LaBiFe_2O_6$ double perovskite has been synthesized by the modified Pechini method. Results of the crystalline characterization through Rietveld analysis of XRD patterns revealed that this material belong to the perovskite family and crystallizes in an orthorhombic structure, *Pnma* (#62) space group. Despite containing two types of cation **(La^{3+} and Bi^{3+})** on sites A and A' of the structure, the proximity between values of their ionic radii and their little magnetic character facilitates this material adopts a structure typical of simple perovskites. The crystallite size studied from the analysis of experimental data of XRD and the average grain size analyzed by SEM images revealed the nanometric nature of the particles forming this double perovskite. EDX spectrum showed that the compound has only the elements which were initially established through its nominal stoichiometry. Magnetic susceptibility measurements as a function of the temperature allowed observing the occurrence of magnetic irreversibility between the ZFC and FC procedures, which are attributed to the crystalline anisotropy related to octahedral distortions that are evident in the material structure. This was determined by the results of magnetization as a function of applied magnetic field that the material behaves like a ferromagnetic at room temperature, with a marked tendency superparamagnetic, which linearizes the saturation regime of the hysteresis curve. This interpretation is corroborated by the results of Mössbauer spectroscopy, which reveals a significant fraction of superparamagnetism mixed with the ferromagnetic response. The superparamagnetic feature is attributed to the nanometric nature of the granular morphology. Finally, the diffuse reflectance measurements suggest that this material behaves as a semiconductor energy gap of *2.17 eV*. In general, the results obtained for samples produced by the modified Pechini method differ from those solid reacted in its magnetic properties related to the average grain size, because this technique allows the obtaining of grains with sizes of nanometric order, with ferromagnetic and superparamagnetic characteristics, which may have applications in biomedicine[24], as sensor in microfluids to facilitate medical diagnoses[25] and for water purification[26,27], between others.

5. Acknowledgments

This work was partially financed by DIB (National University of Colombia - Bogotá) and by CODI (Universidad

de Antioquia - Medellin, Colombia) through Solid Sate Group-GES Sustainability Strategy 2016-2017.

6. References

1. Pechini MP, inventor; Sprague Electric Co, assignee. *Method of preparing lead and alkaline earth titanates and niobates and coating method using the same to form a capacitor*. United States patent US 3330697. 1963 Aug 26.

2. Wu YT, Wang XF, Yu CL, Li EY. Preparation and Characterization of Barium Titanate ($BaTiO_3$) Nano-Powders by Pechini Sol-Gel Method. *Materials and Manufacturing Processes*. 2012;27(12):1329-1333.

3. Del Toro R, Hernández P, Díaz Y, Brito JL. Synthesis of $La_{0.8}Sr_{0.2}FeO_3$ perovskites nanocrystals by Pechini sol-gel Method. *Materials Letters*. 2013;107:231-234.

4. Barrera EW, Pujol MC, Cascales C, Zaldo C, Park KH, Choi SB, et al. Spectroscopic characterization of sol-gel synthesized Tm:Lu_2O_3 nanocrystals. *Applied Physics D*. 2012;106(2):409-417.

5. Jaramillo PJA, Landínez Téllez DA, Roa-Rojas J, Parra Vargas CA, Barrera EW. Synthesis of $LaYbO_3$ perovskite through modified Pechini method: Structural, electric and magnetic characterization. *International Journal of Modern Physics B*. 2015;29(30):1550217.

6. Zhu Z, Tao Z, Bi L, Liu W. Investigation of $SmBaCuCoO_{5+\delta}$ double-perovskite as cathode for proton-conducting solid oxide fuel cells. *Materials Research Bulletin*. 2010;45(11):1771-1774.

7. Tuza PV, Souza MMVM. Steam Reforming of Methane Over Catalyst Derived from Ordered Double Perovskite: Effect of Crystalline Phase Transformation. *Catalysis Letters*. 2016;146(1):47-53.

8. Woodward PM. Octahedral Tilting in Perovskites. I. Geometrical considerations. *Acta Crystallographica Section B*. 1997;53:32-43.

9. Beltrán Rodríguez R, Landínez Téllez D, Roa-Rojas J. Chemical Stability and Crystallographic Analysis of the Sr_2HoNbO_6 Cubic Perovskite as Potential Substrate for $YBa_2Cu_3O_{7-\delta}$ Superconducting Films. *Materials Research*. 2016;19(4):877-881.

10. Cuervo Farfán JA, Aljure García DM, Cardona R, Arbey Rodríguez J, Landínez Téllez DA, Roa-Rojas J. Structure, Ferromagnetic, Dielectric and Electronic Features of the $LaBiFe_2O_6$ Material. *Journal of Low Temperature Physics*. 2017;186(5-6):295-315.

11. Larson AC, Von Dreele RB. *GAS General Structure Analysis System*. Los Alamos: Los Alamos National Laboratory; 2000.

12. Lagarec K, Rancourt DG. *Recoil-Mössbauer Spectral Analysis Software for Windows*. Ottawa: University of Ottawa; 1998.

13. Lufaso MW, Woodward PM. Prediction of the crystal structures of perovskites using the software program SPuDS. *Acta Crystallographica B.* 2001;57(Pt 6):725-738.

14. Kraus W, Nolze G. POWDER CELL - a program for the representation and manipulation of crystal structures and calculation of the resulting X-ray powder patterns. *Journal of Applied Crystallography*. 1996;29(Pt 3):301-303.

15. Lufaso MW, Barnes PW, Woodward PM, Structure prediction of ordered and disordered multiple octahedral cation perovskites using SPuDS, *Acta Crystallographica B*. 2006; 62(3): 397-410.

16. Sasaki S, Prewitt CT, Bass JD, Schulze WA. Orthorhombic perovskite $CaTiO_3$ and $CdTiO_3$: structure and space group. *Acta Crystallographica Section C*. 1987;43(Pt 9):1668-1674.

17. Wondratschek H. Special topics on space groups. In: Arroyo M, ed. *International Tables for Crystallography*. Volume A: Space-group symmetry. Dordrecht: Springer; 2006. p. 732-740.

18. Glazer AM. Simple ways of determining perovskite structures. *Acta Crystallographica Section A*. 1975;31(Pt 6):756-762.

19. Fujii T, Matsusue I, Nakanishi M, Takada J. Formation and superparamagnetic behaviors of $LaFeO_3$ nanoparticles. *Hyperfine Interactions*. 2012;205(1-3):97-100.

20. Morales LA, Sierra-Gallego G, Barrero CA, Arnache O. Relative recoilless F-factors in $REFeO_3$ (RE = rare-earth La, Pr, Nd and Sm) orthoferrites synthesized by self-combustion method. *Materials Science and Engineering: B*. 2016;211:94-100.

21. Sorescu M, Xu T, Hannan A. Initial Stage Growth Mechanism of $LaFeO_3$ Perovskite through Magnetomechanical Ball-Milling of Lanthanum and Iron Oxides. *American Journal of Materials Science*. 2011;1(1):56-66.

22. Kumar V, Sharma SK, Sharma TP, Singh V. Band gap determination in thick films from reflectance measurements. *Optical Materials*. 1999;12(1):115-119.

23. Sorescu M, Xu T, Burnett JD, Aitken JA. Investigation of $LaFeO_3$ perovskite growth mechanism through mechanical ball milling of lanthanum and iron oxides. *Journal of Materials Science*. 2011;46(20):6709-6717.

24. Kumar A, Rai RC, Podraza NJ, Denev S, Ramirez M, Chu YH, et al. Linear and nonlinear optical properties of $BiFeO_3$. *Applied Physics Letters*. 2008;92(12):121915.

25. Akbarzadeh A, Samiei M, Davaran S. Magnetic nanoparticles: preparation, physical properties, and applications in biomedicine. *Nanoscale Research Letters*. 2012;7(1):144.

26. Konry T, Bale SS, Bhushan A, Shen K, Seker E, Polyak B, et al. Particles and microfluidics merged: perspectives of highly sensitive diagnostic detection. *Microchimica Acta*. 2012;176(3-4):251-269.

27. Balaure PC, Gudovan D, Gudovan IA. Nanotechnology depollution of heavy metals present in potable water. In: Grumezescu A, ed. *Water Purification*. London: Academic Press; 2017. p. 551-582.